Energy Advances

ROYAL SOCIETY OF CHEMISTRY

PAPER

View Article Online
View Journal

Cite this: DOI: 10.1039/d5ya00371g

Fe-functionalised N-doped $Ti_3C_2T_z$ MXene for the alkaline oxygen reduction reaction

Luc Bouscarrat,[ab] Alex Scrimshire,[c] Paul A. Bingham,[c] Gaurav Gupta,[a] Richard Dawson[ad] and Nuno Bimbo *[ae]

Alkaline fuel cells are promising technologies to decarbonise current energy systems. One of the main advantages they present is that non-expensive metals can be used as catalysts, reducing overall manufacturing costs. A promising family of electrocatalysts for the oxygen reduction reaction, which is the most difficult reaction in most fuel cell systems, are Fe–N–C catalysts, which have shown performance close to platinum-based catalysts. Coupling these with MXenes is a promising alternative, as MXenes can act as supports that will homogeneously disperse the metal species and catalyse the formation of carbon species that increase performance for the ORR. In this paper, we intercalate Fe species and urea in $Ti_3C_2T_z$ MXene and fully characterise the materials using a range of techniques, including Mössbauer spectroscopy. The materials are then tested for the ORR in alkaline media, with one sample (Ti_3C_2-U50-Fe-800) showing excellent performance and stability in 0.1 M KOH, including an onset potential of 0.93 V *vs.* RHE, an electron transfer number of 3.8 at 0.8 V *vs.* RHE, a Tafel slope of 66 mV dec^{-1}, and a small shift of 37 mV for the half-wave potential for linear sweep voltammetry before and after 2000 cycles. This performance is attributed to the high nitrogen content that favourably forms pyridinic N species on this sample, and the MXene support, which disperses the Fe species and catalyses the formation of favourable carbon materials.

Received 19th December 2025,
Accepted 22nd March 2026

DOI: 10.1039/d5ya00371g

rsc.li/energy-advances

Introduction

Current energy systems are proven to be harmful to the planet, with the most visible impacts being anthropogenic climate change and destruction of ecosystems.[1] This is due to our reliance on fossil fuels, which as of 2023 are still 80% of worldwide primary energy demand.[2] Fossil fuels are inherently limited on the Earth's crust, and their extraction, production and use emits a range of harmful chemicals to the environment. The current state of affairs has prompted governments and organisations worldwide to commit to low-carbon and net-zero technologies, with a view of mitigating many of the effects we are currently seeing from our energy usage. It is in this context that hydrogen has gained momentum as a technology that can help decarbonise sectors, given its many attributes. Hydrogen is the chemical fuel with the highest energy density per unit mass, does not release any harmful chemicals when combusted, and benefits from having several sustainable and clean pathways for production, storage and use.[3] However, there are still many issues associated with hydrogen use, mostly the cost of deploying the technology. According to a recent study, hydrogen should be deployed strategically in areas where it has the greatest potential for cost reduction and sustainability, especially when compared to other low-carbon technologies.[4] Over the past decade, there have been a great number of areas highlighted for hydrogen deployment. Currently, hydrogen seems to have the upper hand over other low-carbon technologies in decarbonising petrochemicals and fertilisers, steelmaking, heavy transport, and as a long-duration energy storage method.[4]

To be able to facilitate hydrogen deployment, cost reductions are essential, and there is much research and development ongoing in all areas of hydrogen technologies. One area that could greatly benefit from cost reductions are fuel cell technologies. Hydrogen is typically coupled with fuel cells, as these can be two to three times more efficient than internal combustion engines.[5] However, fuel cells are costly technologies, as some types require expensive metals such as platinum, which can account for up to 40% of the total cost of the fuel cell.[5] Alkaline fuel cells (also called anion exchange membrane fuel cells or alkaline anion exchange membrane fuel cells) on the other hand can use non-precious metals as catalysts, which can significantly lower their cost.[5] There are two half-reactions taking place in a fuel cell, the hydrogen

[a] School of Engineering, Gillow Avenue, Lancaster University, LA1 4YW, UK
[b] AFC Energy PLC, Dunsfold Park, Canada Avenue, Cranleigh GU6 8TB, UK
[c] School of Engineering and Built Environment, Sheffield Hallam University, City Campus Howard Street, Sheffield S1 1WB, UK
[d] LiNa Energy, White Cross Industrial Estate, South Rd, Lancaster LA1 4XQ, UK
[e] School of Chemistry and Chemical Engineering, Highfield Campus, University of Southampton, Southampton SO17 1BJ, UK. E-mail: n.bimbo@soton.ac.uk

oxidation reaction (HOR) in the anode and the oxygen reduction reaction (ORR) in the cathode. The ORR is the limiting reaction in hydrogen fuel cells due to its sluggish kinetics, meaning that developing catalysts that have good activity and stability for this reaction is of primary concern for reliable and affordable fuel cell technologies.[5] The ORR in alkaline fuel cells benefits from the availability of a wider range of catalyst materials than acidic media, meaning expensive catalysts such as platinum group metals can be avoided. The ORR can proceed with a two electron or a four-electron pathway, as described by the following reactions:

$$O_2 + H_2O + 2e^- \rightleftharpoons HO_2^- + OH^- \quad (1)$$

$$HO_2^- + H_2O + 2e^- \rightleftharpoons 3OH^- \quad (2)$$

$$O_2 + 2H_2O + 4e^- \rightleftharpoons 4OH^- \quad (3)$$

In the equations above, the top two equations represent the $2e^-$ pathway that involves the formation of peroxide ions and a possible further reduction to OH^-. The equation at the bottom represents the $4e^-$ pathway reduction to OH^-. Many electrocatalysts have been suggested for the ORR in alkaline media, with dispersed metals in N-doped carbons (M–N–C catalysts) recently emerging as a promising solution. Some of these catalysts exhibited performances that approached those of platinum group metals for the ORR. Among these, Fe-based catalysts (Fe–N–C), which typically consist of a N-doped carbon support containing Fe–N_x moieties, have been investigated and shown good selectivity for the $4e^-$ pathway.[5]

MXenes are a new class of two-dimensional materials discovered in 2011.[6] They consist of transition metal carbides, carbonitrides, or nitrides, and they have shown much promise in a range of areas, including electrochemical and catalytic applications, electromagnetic shielding, and electronic applications, among many others.[7] MXenes have been used as electrocatalysts for the ORR, and they have shown to adsorb oxygen-containing species, which is a positive factor that influences performance.[8,9] There have been several studies that assessed ORR activity in MXenes using both Pt and non-PGM metals.[9] M–N–C structures (where M can be Fe or Co) supported on MXenes have also been tested, showing performance in the ORR close to that of Pt-based catalysts.[10] This is linked to the quantity of nitrogen atoms that form coordination bonds with the transition metal centre, with the M–N_4 arrangement looking like the most favourable.[10] This led to several studies attempting to couple MXenes with M–N–C materials. Li *et al.* designed a catalyst with Fe–N_4 moieties and $Ti_3C_2T_z$ (where T_z stands for surface terminations such as –F, –O and –OH) using iron phtalocyanine and evaluated ORR activity.[11] The conclusion was that this combination resulted in a reduction of the work function of Fe centres, leading to enhanced ORR activity. Other studies such as the one by Wang *et al.*[12] looked at Co-CNT forming on MXene structures and again showed good ORR activity. There are also other reports of non-precious metal electrocatalysts deposited in MXenes in alkaline electrolytes, including Co,[13] Fe–N–C,[14–16] Fe–Co,[17] Co_3O_4/NCNTs,[18] Mn_3O_4,[19] $NiCo_2O_4$,[20] MoS_2,[21] CoS_2,[22] and g-C_3N_4.[23]The fact that M–N–C catalysts supported on MXenes, especially Fe species, can show performance for the ORR close to Pt-based catalysts, is a promising sign for alkaline fuel cells that do not rely on expensive platinum group metals. Other recent developments on MXenes for the ORR have focussed on doping and defect engineering to enhance performance.[24–26] Several non-metallic dopants have been investigated, including boron, oxygen, chlorine, bromine, iodine, sulfur and others.[25] Nitrogen doping has also proven quite popular, and N-doped MXenes have been used as electrocatalysts for hydrogen production, in both the hydrogen evolution and oxygen evolution reactions.[26]

In this paper we develop a strategy that intercalates a Fe precursor and urea between the MXene layers, and test the resulting materials for the ORR. The urea will act as a C and N source, and the materials will subsequently be thermally annealed. The Fe precursor is expected to form iron species such as Fe, Fe_3C and/or Fe–N_x, all of which have shown good ORR activity in alkaline media, and the expectation is that the layered nature of MXenes will help disperse the Fe-species homogeneously on the material. In addition, there is the possibility that Fe species catalyse the formation of carbon compounds from the decomposition of urea on the surface of the MXenes, such as carbon nanofibres or nanotubes, which are also promising materials to catalyse the ORR.

Experimental section

Synthesis of $Ti_3C_2T_z$

The etching procedure for $Ti_3C_2T_z$ is the LiF–HCl etching method, which is adapted from Ghidiu *et al.*[27] and has been reported before.[28–30] Recently, a procedure based on this method was used for semi-continuous synthesis of Ti_3C_2.[31] Ti_3AlC_2 MAX phase (>85% purity) was bought from Carbon-Ukraine Ltd (Kyiv, Ukraine) and was ground and sieved through a −400 mesh sieve. The etching procedure was then done but adding 3 g of LiF (99%, Alfa Aesar) to 30 mL of 6 M HCl (37.5 wt%, Sigma Aldrich) in a HF-resistant beaker. Once the salt was dissolved, 3 g of ground and sieved Ti_3AlC_2 were slowly added to the solution to avoid overheating. The beaker was closed with a lid that had a small hole to allow venting of the H_2 that forms during the reaction. The mixture was left to stir at 40 °C for 48 h. After this, the sample is removed from the beaker and rinsed several times with DI water, using a centrifugation step between rinses of 2000 rpm for 5 min at room temperature. This rinsing procedure was repeated until the pH of the supernatant was above 6. The sample was then left to dry overnight at around 70 °C in a drying oven.

Synthesis of Ti_3C_2-U-Fe-800 and C-U50-Fe-800

The synthesis of Ti_3C_2-U-Fe-800 samples was done by first mixing the MXene with urea in DI water at different weight ratios (1 : 10 and 1 : 50). $FeCl_3 \cdot 6H_2O$ (>99%, Sigma Aldrich) was added to the solution at a 1 : 1 weight ratio to MXene. The solution is then stirred at 55 °C for 15 h and dried afterwards.

The mixture was then ground and transferred to an alumina crucible and thermally treated using a two-step treatment. This treatment was done to degrade urea (550 °C is the reported temperature for urea decomposition) so that it can react with the MXenes and change their surface chemistry. This could also potentially enable urea decomposition products to act as pillars between the MXene layers. Samples were heated in a tube furnace under argon to 550 °C at 5 °C min^{-1} and then left at that temperature for 3 h. After the 3 h, the samples were further heated to 800 °C at 5 °C min^{-1}. Once 800 °C were reached, the temperature was kept for 1 h and then left to cool down back to room temperature. The crucible was covered with an alumina cover to reduce material losses during decomposition of urea. For the synthesis of C-U50-Fe-800, the same approach as described above was followed, but the MXene was replaced by carbon black (XC72R, Cabot). To benchmark the electrochemical performance, a sample of commercial Pt on carbon was used (20% Pt on carbon, Johnson Matthey HiSPEC).

Physicochemical characterisation

Powder X-ray diffraction (PXRD) measurements were done on a Rigaku Smartlab diffractometer (Rigaku, Japan) that used Cu Kα as the radiation source (λ = 1.54 Å). The diffractometer was operated on reflection mode using a Bragg–Brentano geometry using a scan rate of 3° min^{-1} between 4° and 50°. ^{57}Fe Mössbauer spectroscopy was performed with a ^{57}Co in Rh source in motion at constant acceleration, at 293 K over a velocity range of ±12 mm s^{-1} using a see Co W304 and W202 drive unit and a 1024 channel spectrometer. Samples were loaded into a Perspex sample holder which is gamma-ray transparent and natural alpha-Fe was used to calibrate the velocity scale. Scanning electron microscopy (SEM) was done using a JEOL JSM-7800F (JEOL, Japan) with an acceleration voltage of 5 or 10 kV and a working distance of 10 mm. Energy-dispersive X-ray spectroscopy (EDS) was done using a X-Max50 (Oxford Instruments, Abingdon, UK) using an accelerated voltage of 10 kV and a working distance of 10 mm. For both SEM and EDS, samples were dry cast on a carbon tape support, which was placed on top of a copper stub. Gas sorption measurements were done on a Micromeritics 3Flex (Micromeritics Instrument Corporation, Georgia, USA) using high-purity nitrogen gas at 77 K. The specific surface areas were calculated from the nitrogen adsorption isotherms using the BET method, over a relative pressure P/P_0 window of 0.05 to 0.15. Pore size distributions were calculated using the software on the instrument, which employed the NLDFT method (non-local density functional theory), a common method to determine pore size distributions, using a slit pore model. X-ray photoelectron spectroscopy (XPS) was done using a Thermo Fisher Scientific NEXSA spectrometer with a micro-focused monochromatic Al X-ray source (19.2 W) over an area of approximately 100 μm. The data were recorded with pass energies of 150 eV in survey scans and 40 eV for high-resolution scans using a step size of 1 and 0.1 eV, respectively. Charge neutralisation was obtained using a combination of both low energy electrons and argon ions, and cluster cleaning was performed with 2 keV energy at 0.5 × 0.5 mm area for 60 s to remove surface contamination. Details of the XPS peak fitting are in SI.

Electrochemical characterisation

Electrochemical characterisation of the samples was done at room temperature using a Pine Instruments (Pine Research Instrumentation, Durham, USA) rotating disk electrode/rotating ring disk electrode (RDE/RRDE) with a modulated speed rotator. A glassy carbon (GCE) disk RRDE tip (disk diameter of 5.61 mm) and a platinum ring (ring outer diameter of 7.92 mm) were used as the working electrode, a saturated calomel electrode (SLS, Nottingham, UK) was used as a reference electrode and a coiled Pt wire was used as the counter electrode.

The samples were prepared as follows: 5 mg of catalyst powder were added to 480 μL of absolute ethanol and 20 μL of Nafion solution (5 wt%), which was then ultrasonically dispersed for 30 min to form a homogeneous ink (ultrasonication was stopped to change the water frequently so that the temperature did not rise above 35 °C). The working electrode was polished with an alumina slurry (Ø of 0.3 μm) and was subsequently bath sonicated for 5 min, rinsed with DI water and left to dry. Then, 10 μL of the catalyst ink were spincast on the GCE while rotating at 500 rpm to give an homogeneous coating on the electrode, so that the desired mass loading of catalyst was obtained (~0.40 mg cm^{-2}). The electrode was then left to dry for 30 min in air prior to running the electrochemical experiment. Prior to any testing, cyclic voltammetry was performed on the samples at a scan rate of 50 mV s^{-1} in the 0.1 to 1 V *vs.* RHE potential window under nitrogen flow to activate the catalyst.

The RDE tests were performed using linear sweep voltammetry (LSV) running an anodic sweep between the 0.1 and 1.1 V *vs.* RHE potential window, with electrode rotation speeds ranging from 400 to 1600 rpms at a scan rate of 5 mV s^{-1} in nitrogen and air. The LSVs have been *iR* and background corrected, the N_2 component was subtracted and the current has been normalized to the geometrical surface area of the working electrode (0.247 cm^2). The tests were done in a 0.1 M aerated KOH electrolyte. Using an oxygen-saturated electrolyte would lead to better performance in all samples but we have opted to use air-saturated electrolytes, as this would mirror performance in real-world applications more closely, as air is more likely to be used than pure oxygen. To determine the *iR* correction, electrochemical impedance spectroscopy was performed prior to the measurement (not shown) and the value for the real part of the impedance at high frequency in the Nyquist plot was used for the correction. To convert potential measured *vs.* SCE (saturated calomel electrode) against RHE, the following equation was used:

$$E_{RHE} = E_{SCE} + 0.059 \times pH \times 0.2445 \quad (4)$$

RRDE measurements were performed using LSV at an anodic sweep between a potential window of 0.1 and 1.1 V *vs.* RHE (disk) at 1600 rpm at a scan rate of 5 mV s^{-1} while the ring was

held at a potential of 1.3 V *vs.* RHE. The electron transfer number n and the H_2O_2 yield can be determined from the disk and ring current measurements using the following equations:

$$n = \frac{4I_d N}{I_d N + I_r} \quad (5)$$

$$\%H_2O_2 = 100\frac{2I_r N}{I_d N + I_r} \quad (6)$$

where n is the electron transfer number, I_d is the disk current, N is the collection efficiency, I_r is the ring current and $\%H_2O_2$ is the hydrogen peroxide yield. The Levich equation is routinely used to analyse electrochemical performance, and can be represented as:

$$j_L = 0.201nFC_0D_0^{2/3}\nu^{-1/6}\omega^{1/2} \quad (7)$$

where j_L is the current density, n is the electron transfer number of the reaction, F is Faraday's constant, C_0 is the concentration of oxygen in solution, D_0 is the diffusion coefficient of oxygen in solution, ν is the kinematic viscosity of the electrolyte and ω is the rotation speed of the electrode in rpm. The electron transfer number can be obtained from the Koutecky–Levich equation, which relates the measured current j to the kinetic current j_k and the limiting current j_l:

$$\frac{1}{j} = \frac{1}{j_k} + \frac{1}{j_l} \quad (8)$$

If we introduce the Levich equation in the above, we get:

$$\frac{1}{j} = \frac{1}{j_k} + \frac{1}{B_L}\omega^{-1/2} \quad (9)$$

where the Levich equation becomes:

$$B_L = 0.201nFC_0D_0^{2/3}\nu^{-1/6} \quad (10)$$

where B_L is current density, n is the electron transfer number, F is Faraday's constant, C_0 is the concentration of oxygen in solution, D_0 is the diffusion coefficient of oxygen in solution, ν is the kinematic viscosity of the electrolyte and ω is the rotation speed of the electrode in rpm. The Koutecky–Levich plot (KL) can be obtained by plotting j^{-1} *vs.* $\omega^{-1/2}$ and $1/B_L$ can be determined from the slope of the curve. Accelerated durability testing (ADT) was done by cycling the samples on a potential window between 0.5 and 1 V *vs.* RHE for 2000 cycles, sweeping at a 50 mV s^{-1} rate in an electrolyte which is a 0.1 M aerated KOH solution.

Results and discussion

As detailed in the introduction, the aim is to intercalate a Fe precursor and urea between the MXene layers and anneal the material. The precursor $FeCl_3$ is expected to form iron species such as Fe, Fe_3C and Fe–N_x, all of which have shown good ORR performance in alkaline media. In addition to the catalytic activity for the ORR, the Fe will also act as a catalyst for the formation of carbon species between the MXene layers, which result from urea decomposition at high temperatures. Additionally, the layered nature of MXenes and their capacity to be intercalated by cations will allow for intercalation of Fe species from the precursor, and ideally result in a homogeneous distribution of Fe-species on the support.

The different samples were analysed with powder X-ray diffraction (PXRD) to study the effect of the Fe precursor, and to evaluate the crystalline phases that are present in the materials. The PXRD pattern for the precursor MAX phase and synthesised MXene are in SI, Fig. S1. The MXene : urea ratios were 1 : 10 and 1 : 50, as these were considered optimal.[32] To benchmark the results, a sample that uses carbon black (XC72R) was also used as support and applied the same treatment (sample C-U50-Fe-800). Fig. 1 shows the powder X-ray diffraction patterns of the samples.

As seen in Fig. 1, the sample C-U50-Fe-800 shows most of the distinct peaks that are characteristic of the Fe_3C phase.[33] However, there are extra peaks at 44.5°, 44.9°, and 65.0°. Both these peaks can be explained by the presence of α-Fe, as the (110) and (200) planes of α-Fe have peaks at 44.5° and 65.0°. There is another broad peak visible at 25.0°, which is characteristic of amorphous carbon present in XC72R carbon black.

For the MXene-supported samples, Ti_3C_2-U10-Fe-800 and Ti_3C_2-U50-Fe-800, both have the same Fe_3C and α-Fe peaks as

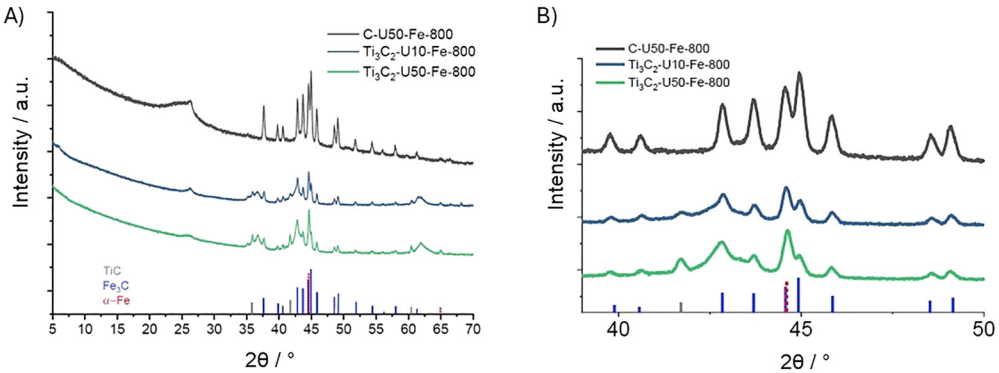

Fig. 1 Powder X-ray diffraction patterns for the Ti_3C_2-U10-Fe-800, Ti_3C_2-U50-Fe-800, and C-U50-Fe-800 samples. (A) Diffractogram for Ti_3C_2-U10-Fe-800, Ti_3C_2-U50-Fe-800, and C-U50-Fe-800 samples. Lines on the *x*-axis are the main peaks for TiC, Fe_2C and α-Fe. (B) Same pattern as (A) between 39 and 50°.

the C-U50-Fe-800 sample. The intensity ratios of the peaks at 44.5° and 44.9° differ between samples, as expected, since the composition of the Fe phases will vary according to the different amounts of urea. A small peak at 25.0° is also visible, indicating the presence of graphitic carbon in the sample. It should be noted that the PXRD results do not show any peaks related to TiO_2 rutile or anatase,[34] meaning that the MXenes have not been oxidised into these species with the thermal treatment. Peaks are also present at 35.9°, 41.7°, and 60.5°, most likely resulting from impurities in the starting materials (TiC) and surface degradation, and at 36.6°, 42.9°, and 61.7°, which could be from MXene layer rearrangement or from the titanium nitride that could be formed on the surface during the thermal step. Finally, the characteristic (002) peak from MXenes does not seem to be present, but it is unlikely that the MXene structure has completely degraded. The most probable explanation for the absence of the peak is the formation of extra carbonaceous species between the MXene layers, which have disordered the MXene structure along the (002) direction. Fig. 1B shows the XRD patterns between 39.0° and 50.0° to gain insight into the composition of Fe-species in the samples. The figure shows the difference in intensity of the 44.5° and 44.9° peaks, indicating a distinct distribution of the Fe-species in the samples, implying that it depends on both the amount of urea and the type of support that is used. Rietveld analysis is done on the XRD patterns, and the Fe_3C/α-Fe ratios are determined and shown in Table 1.

The highest proportion of Fe_3C is obtained in the sample that contains XC72R, which can be explained by the presence of more carbon available to react. It is known that MXenes easily interact with cations, leading in many cases to spontaneous intercalation between the layers. In this case, Fe could intercalate the MXene layers, and thus stopping it from reacting to form Fe_3C, explaining the lower Fe_3C content relative to Fe. More characterisation of the samples, including elemental analysis, is included in SI, in Fig. S2, and Table S1.

It is important to determine the Fe content, and powder XRD is a technique that is inadequate for this purpose, so a more suitable analytical technique is required. ^{57}Fe Mössbauer spectroscopy has the advantage of being able to detect all the Fe in a sample, regardless of its physical state, and the signal is directly proportional to the amount of Fe-species the sample contains. The fitted experimental ^{57}Fe Mössbauer transmission spectra are shown in Fig. 2, with fitting parameters included in SI (Tables S2–S4).

Fig. 2 shows the fitted Mössbauer spectra, with the spectra of all three samples satisfactorily deconvoluted into one doublet and two sextets. Details of this deconvolution can be found in SI. Based on literature,[35–37] the doublet has been attributed to Fe–N_x species usually observed in N-doped carbon materials that contain Fe, and where Fe forms Fe–N_x moieties with four pyridine-like nitrogen on the carbon layer, as shown in Fig. 2D. Fe–N_x species cannot be identified by XRD, as they are non-crystalline. Sextets 1 and 2 are attributed to α-Fe and Fe_3C, respectively, in agreement with the XRD results discussed earlier. The Fe-species compositions are given in Table 2 and are broadly consistent with the XRD results. In fact, the Fe_3C/α-Fe ratios are similar to those calculated by Rietveld analysis and broadly follow the same trend. In addition to the Fe_3C and α-Fe increases discussed before, the content of Fe–N_4 in the sample also increases with the amount of urea, which can be explained by the greater availability of nitrogen to form these moieties. On the other hand, the Fe–N_x content for the XC72R sample decreases considerably and amounts to only 7% of the Fe-species. This can be explained by the spatial confinement that MXene layers bring to Fe ions and urea, inhibiting the agglomeration of Fe into bigger particles during thermal treatment, which allows for more Fe to react and form Fe–N_x moieties.

To further characterise the morphology of the samples and their porosity, SEM and nitrogen adsorption were used. The results and analysis are in SI in Fig. S3 and S4, showing that carbon nanotubes and carbon nanofibres are formed on the materials, and that the materials have BET surface areas of 124.1 $m^2\ g^{-1}$ and 178.5 $m^2\ g^{-1}$, for the Ti_3C_2-U50-Fe-800 and Ti_3C_2-U10-Fe-800 respectively. Sample C-U50-Fe-800 has a BET surface area of 204.6 $m^2\ g^{-1}$. This is shown in SI, in Fig. S5.

Surface chemistry of the samples is of paramount importance, as the surface/electrolyte interface is where electrochemical reactions occur. For our case, it is especially relevant to see the effect of introducing $FeCl_3$ on the surface chemistry of the different samples. To study the surface chemistry and to better understand the chemical environment at the materials' surface, X-ray photoelectron spectroscopy (XPS) was performed on the samples to study the states of Ti, C, N and Fe. The full XPS spectra is included in SI in Fig. S6, along with the details for the deconvolution of the spectra. Fitting parameters are in SI, in Tables S6–S9. Surface composition determined from the XPS analysis is presented in Table 3. It can be seen in Table 3 that most of the surface composition in all three samples is made up of carbon (>80 at%). There are also significant amounts of oxygen (7–8 at%) and nitrogen (~4–8 at%) in the Fe-treated samples. There are also residual amounts of iron, fluorine and chlorine, the latter likely being surface functional groups on the MXenes resulting from the etching. MXenes' stability is highly influenced by the surface group terminations, with –Cl functional groups showing more stability than –F or =O groups. Acidic environments can accelerate oxidation while alkaline environments can slow it down but, as noted, this is highly dependent on the functional groups present.[38–40] The XC72R carbon black sample (C-U50-Fe-800) has most of the surface covered in carbon (>97 at%), some oxygen (1.50 at%), nitrogen (0.81 at%) and a residual amount of iron (0.06 at%).

Table 1 Fe_3C/α-Fe ratios calculated from PXRD analysis of the [39°–50°] region

Sample	Fe_3C/α-Fe
Ti_3C_2-U10-Fe-800	5.4
Ti_3C_2-U50-Fe-800	3.4
C-U50-Fe-800	16.8

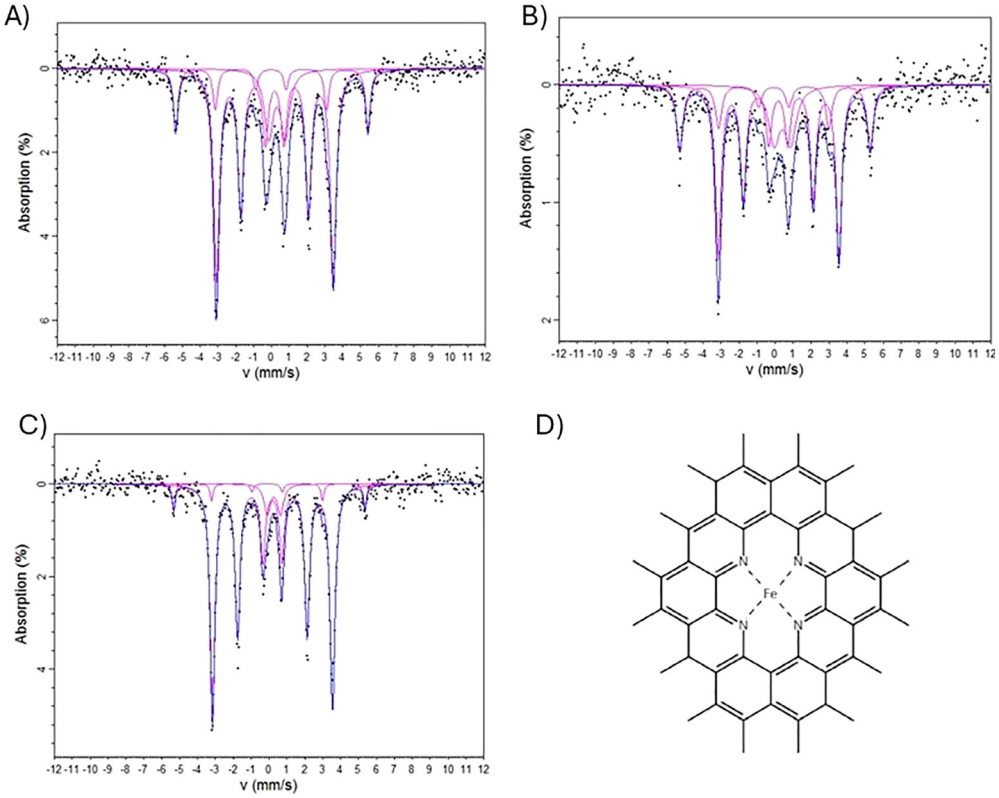

Fig. 2 Fitted experimental ^{57}Fe Mössbauer transmission spectra at 293 K and their respective fittings. (A) Ti_3C_2-U10-Fe-800, (B) Ti_3C_2-U50-Fe-800 and (C) C-U50-Fe-800. (D) Example schematic of Fe–N_4 moiety in carbon materials.

Table 2 Fe-species composition taken from experimental ^{57}Fe Mössbauer analysis of Ti_3C_2-U10-Fe-800, Ti_3C_2-U50-Fe-800 and C-U50-Fe-800

(at%)	Doublet 1 (Fe–N_x)	Sextet 1 (α-Fe)	Sextet 2 (Fe_3C)	Fe_3C/α-Fe
Ti_3C_2-U10-Fe-800	15.8	15.8	68.3	4.3
Ti_3C_2-U50-Fe-800	18.3	23.8	57.9	2.4
C-U50-Fe-800	7.0	6.0	87.0	14.5

Fig. 3 shows the high-resolution XPS spectra for Ti 2p, C 1s, N 1s, and Fe 2p, along with the corresponding fittings, for samples Ti_3C_2-U10-Fe-800, Ti_3C_2-U50-Fe-800, and C-U50-Fe-800. The Ti 2p peak-fitted spectra of Ti_3C_2-U10-Fe-800 and Ti_3C_2-U50-Fe-800, shown in Fig. 3A, displays the typical 2p spin–orbit splitting of titanium. The spectra could be both deconvoluted into 4 components at (455.3 eV/460.4 eV), (456.3/461.2) eV, (457.7/462.8) eV and (458.7/464.4) eV, corresponding respectively to Ti–C, Ti^{2+}, Ti^{3+}, and Ti^{4+}. The variation of the oxidation state of surface Ti shows that there has been a change in the chemical environment at the surface of the MXenes, showing electronic interaction between the MXene support and the Fe-containing carbon structure, which was formed on top of it during the synthesis. The Ti 2p XPS peak fitting distribution parameters for the Fe samples are included in SI in Table S7.

The C 1s spectra of Ti_3C_2-U10-Fe-800, Ti_3C_2-U50-Fe-800, and C-U50-Fe-800 are shown in Fig. 3B, with the spectra deconvoluted into five peaks. The main peak centred at 284.8 eV corresponds to C–C bonds and was attributed to the carbon structures formed on top of the materials. Moreover, there is no obvious C–Ti peak at around 282 eV, which is a peak characteristic from Ti_3C_2, hinting that there is not much MXene at the surface of the samples. A very small shoulder at 283.9 eV is present and is believed to correspond to the C–Fe bond from Fe_3C.[36,41] Based on these results and the elemental composition determined from XPS and shown in Table 3, it can be concluded that apart from small amounts of Ti_3C_2 and Fe species which are still detected as surface species, most of the MXene and Fe species are covered and/or encapsulated in carbon compounds.

Table 3 Surface elemental composition of Ti_3C_2-U*x*-Fe-800 and C-U50-Fe-800 samples from XPS analysis

(at%)	Ti 2p	C 1s (C/Ti)	O 1s	N 1s (N/Ti)	Fe 2p	F 1s	Cl 1s
Ti_3C_2-U10-Fe-800	1.63	85.31 (52.34)	7.51	3.96 (2.4)	0.62	0.24	0.73
Ti_3C_2-U50-Fe-800	2.25	80.09 (35.60)	8.25	7.73 (3.4)	0.57	0.63	0.49
C-U50-Fe-800	—	97.63	1.50	0.81	0.06	—	—

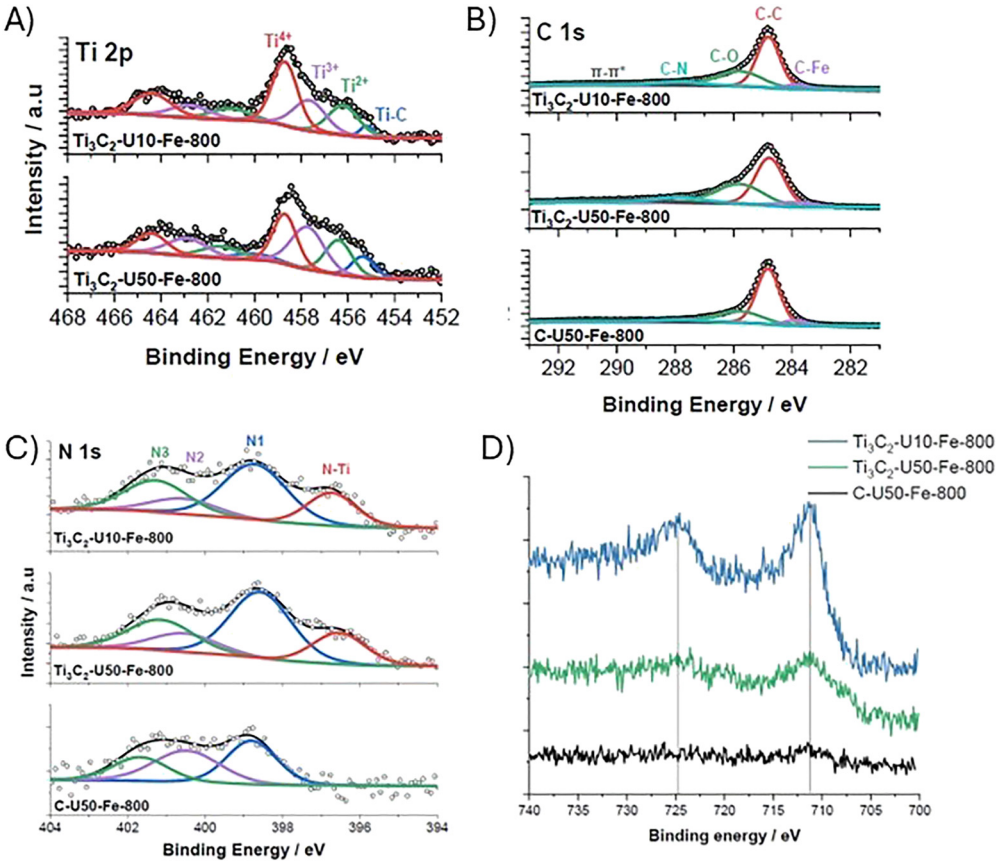

Fig. 3 XPS high-resolution spectra of samples Ti_3C_2-U10-Fe-800, Ti_3C_2-U50-Fe-800, and C-U50-Fe-800. (A) Ti 2p XPS spectra of Ti_3C_2-U10-Fe-800 (top) and Ti_3C_2-U50-Fe-800 (bottom). (B) C 1s XPS spectra of Ti_3C_2-U10-Fe-800 (top), Ti_3C_2-U50-Fe-800 (middle) and C-U50-Fe-800 (bottom). (C) N 1s XPS spectra of Ti_3C_2-U10-Fe-800 (top), Ti_3C_2-U50-Fe-800 (middle) and C-U50-Fe-800 (bottom). (D) Fe 2p XPS spectra of Ti_3C_2-U10-Fe-800 (top), Ti_3C_2-U50-Fe-800 (middle) and C-U50-Fe-800 (bottom).

The chemical state of nitrogen and Fe-species, as well as their local environment on the surface of the materials, are key for catalytic performance towards the ORR. Therefore, both were analysed and deconvoluted. As shown in Fig. 3C, the N 1s spectra of the Fe samples can be deconvoluted into four peaks, with binding energies around 396.4, 398.7, 400.2 and 401.4 eV, which can be assigned to N–Ti bonds, pyridinic N (N1), pyrrolic N (N2) and graphitic N (N3), respectively.[42] The N 1s XPS peak fitting distribution parameters are given in SI in Table S6, where the atomic concentrations of the different N species are presented. The proportion of different N species on the surface of both MXene samples is very similar, even with a urea content that is five times higher. It is also noticeable that the Ti_3C_2-U50-Fe-800 sample contains a bit more pyridinic N and a bit less graphitic N. Based on previous studies, Fe–N_x species usually forms at pyridinic N, where Fe atoms coordinate with pyridinic N,[43,44] meaning that a proportion of the pyridinic N (N1) peak can be attributed to Fe–N_x moieties. Presence of pyridinic N not coordinated to Fe might also exist but the difficulty in deconvoluting the Fe spectra mean quantifying Fe-coordinated and non-coordinated pyridinic N is not possible. The Fe 2p spectra for Ti_3C_2-U10-Fe-800, Ti_3C_2-U50-Fe-800, and C-U50-Fe-800 are presented in Fig. 3D. As the overall XPS signal for Fe is small, there is some noise on the spectra, which made deconvolution difficult. However, peaks are still visible in the spectra of Ti_3C_2-U10-Fe-800 and Ti_3C_2-U50-Fe-800, which are at 711.5 eV and 724.9 eV. The Fe 2p peak at 711.5 eV probably corresponds to Fe^{2+}, which is inherent to Fe–N_x species as noted in the literature.[45,46]

The two main objectives of introducing $FeCl_3$ during the synthesis were to increase the overall surface area of our materials and to introduce species which could improve activity of the materials towards ORR. The synthesized materials show increases in surface area and a greater carbon and nitrogen content, in addition to formation of Fe-species such as Fe_3C, α-Fe and Fe–N_4, all of which have shown interesting ORR properties in alkaline media.[47] Also, based on the XRD, ^{57}Fe Mössbauer spectroscopy, and SEM results, the choice of support plays a role in the morphology of the materials and on the chemistry of the Fe-species that are synthesised. The influence of the different parameters, such as the introduction of $FeCl_3$, the use of Ti_3C_2 and XC72R as different supports, and the amount of urea in the MXene samples, needs to be related to the electrochemical performance of the synthesised materials. As such, electrochemical characterisation was done on the samples to determine the electrochemical activity and to relate

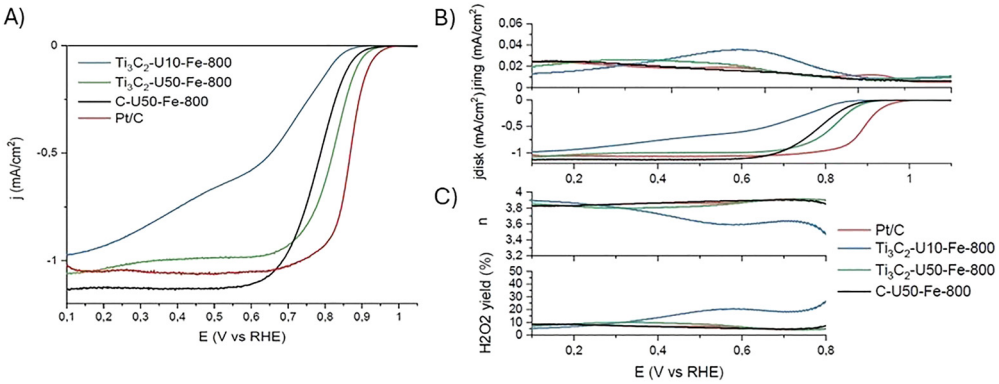

Fig. 4 (A) Linear sweep voltammogram at 5 mV s^{-1} of the different samples in 0.1 M aerated KOH electrolyte (corrected) at 1600 rpm. (B) Rotating ring disk electrode measurements of the different Ti_3C_2-Ux-Fe-800 samples, C-U50-Fe-800, and Pt/C in 0.1 M aerated KOH electrolyte (corrected) at 1600 rpm and scan rate of 5 mV s^{-1}: j_{disk} (bottom) and j_{ring} (top), (C) calculated H_2O_2 yield (bottom) and electron-transfer number n (top) for Ti_3C_2-Ux-Fe-800 samples, C-U50-Fe-800, and Pt/C.

it with the different physico-chemical properties. Linear sweep voltammetry (LSV) and rotating ring disk electrode (RRDE) measurements were performed on the samples and are presented in Fig. 4.

In the figure, electrochemical characterisation was done using linear sweep voltammetry (LSV) in a rotating disk electrode (RDE) at 1600 rpm. The LSV curves were measured in the 0.1 to 1.1 V (*vs.* RHE) potential range using a 0.1 M aerated KOH electrolyte. Results are shown in Fig. 4A for Ti_3C_2-U10-Fe-800, Ti_3C_2-U50-Fe-800, and C-U50-Fe-800. A well-known benchmark catalyst for ORR activity was also tested and compared (20% Pt/C). It should be noted that standard calomel electrodes, the reference electrode used for these tests, have been shown to leak Cl^- ions into solution, which could affect performance of Pt electrodes. MXene samples would be less likely to suffer from drawbacks in performance from Cl^- ions, since they are synthesised using HCl and, as shown in the elemental analysis, Cl is already present in the samples.

From the LSV curves performed at 1600 rpm presented in Fig. 4A, it can be seen that for samples Ti_3C_2-U50-Fe-800 and C-U50-Fe-800, the ORR has reached mass transport limitation at potentials below 0.6 V *vs.* RHE, while at potentials higher than 0.6 V *vs.* RHE, the curve is dictated by a mixed region, where both kinetics and diffusion play a role. In the case of Pt/C, the potential at which the mass-transport region is attained is 0.7 V *vs.* RHE, owing to better ORR performance. On the other hand, the LSV for Ti_3C_2-U10-Fe-800, although getting close to theoretical limiting current values, does not reach a plateau at any potential.

The main parameters that can be determined from LSV include onset potential (E_{onset}), half-wave potential ($E_{1/2}$), and the diffusion-limiting current density (j_L). The onset potential is a parameter which can give a first idea of how active a catalyst is towards ORR, as it is the specific electrode potential at which the oxygen reduction begins to occur, which is marked by a rapid increase in current. Indeed, a greater onset potential means that a smaller overpotential is required to overcome the energy needed to start the ORR. With respect to onset potential (E_{onset}), Pt/C shows the highest value at 0.96 V *vs.* RHE, owing to its excellent activity towards the ORR. The onset potential for all three synthesized samples (Ti_3C_2-U10-Fe-800, Ti_3C_2-U50-Fe-800 and C-U50-Fe-800) are lower than Pt/C, at potential values of 0.86, 0.93 and 0.91 V *vs.* RHE, respectively. It can also be seen that using Ti_3C_2 as a support has helped improve the onset potential compared to the sample using XC72-R. This could be explained by the fact that using Ti_3C_2 as support promoted the formation of Fe–N_x moieties, which have shown to have outstanding electrochemical activity towards ORR, especially when coupled with Fe_3C and α-Fe.[33,47–50] On the other hand, Ti_3C_2-U10-Fe-800 also displays a higher content of Fe–N_x compared to C-U50-Fe-800, but out of all three samples synthesized, Ti_3C_2-U10-Fe-800 is the one with the poorer onset potential. One possible explanation could be the difference in morphology of Ti_3C_2-U10-Fe-800, which was the only sample that did not grow CNT/CNF-like carbon structures.

Some variation in limiting current density is observable between Ti_3C_2-U50-Fe-800, C-U50-Fe-800 and Pt/C. As noted before, in the Levich equation the limiting current density does not depend on the intrinsic properties of the catalyst, except for n, which is the number of electrons exchanged during the reaction. Looking at the figure, it seems that the Ti_3C_2-U10-Fe-800 could have some mixed ORR processes happening during the electrochemical testing, as the LSV displays two reduction waves, denoted by the shoulder on the LSV at potential 0.6 V *vs.* RHE. This could be indicative of two different active sites which would participate towards ORR at different potentials. The higher limiting current density on the C-U50-Fe-800 compared to the Pt/C sample might be due to small defects on the surface of the electrode and/or the non-uniform coating of catalyst on the working electrode surface. We also note that the limiting current density for Pt/C at 1600 is below typical values of 5–6 mA cm^{-2}, which is due to the use of aerated electrolytes rather than commonly used oxygen-saturated ones.

RRDE measurements, as well as the calculated peroxide yield and electron transfer number, were also done on all samples and are presented in Fig. 4B and C. The RRDE of Pt/C

is characteristic, with a slight increase of j_{ring} at lower potential. The peroxide formation is below 10% throughout the potential window and the calculated transfer number ranges between 3.8 and 3.9. Thus, it is clear that Pt/C catalyses the ORR mostly through a 4-electron process. In the case of C-U50-Fe-800, the evolution of j_{ring} is very similar to Pt/C, as the ring current density barely increases at lower potentials, which yields a small amount of peroxide during the testing. The electron transfer number also ranges around 3.8 and 3.9 for this sample. Ti_3C_2-U50-Fe-800 displays a ring current density which increases slightly more than the two previous samples around 0.4 V *vs.* RHE. The electron transfer number is evaluated at around 3.8 using RRDE for Ti_3C_2-U50-Fe-800, which is higher than the value of 3.66, but is still reasonably within error. Out of all the samples, only Ti_3C_2-U10-Fe-800 shows a noticeable increase in j_{ring} during the first reduction wave, owing to peroxide formation. The ring current density then decreases during the second reduction wave of the LSV. This shows that the ORR reaction on the surface of Ti_3C_2-U10-Fe-800 partially happens through a 2-electron pathway, forming peroxide that could be detected on the ring but would be further reduced to OH^- at a lower potential. The samples were further characterised using the same sweep rate (5 mV s^{-1}) and conditions [0.1 M aerated KOH electrolyte (corrected)] but at different rotation speeds, ranging from 400 to 1600 rpm. The results and corresponding Koutecky–Levich (KL) plots are presented in Fig. 5.

The K–L plots show good parallelism and linearity, indicating first-order reaction kinetics. The calculated electron transfer number for all the samples at potentials 0.4, 0.5, 0.6, 0.7 and 0.8 is given in the legends of the K–L plots. As expected, the sample with the highest electron transfer number is Pt/C (Fig. 5G and H), with an average value of 3.91 over the potential used to plot the K–L curves. Samples Ti_3C_2-U50-Fe-800 (Fig. 5E and F) and C-U50-Fe-800 (Fig. 5C and D) have an average similar electron transfer number of 3.66 and 3.69, respectively. But the evolution of n differs for the two samples, as both show a stable value of n between the potentials 0.4 and 0.7 V *vs.* RHE, but the value of the electron transfer number increases at 0.8 V *vs.* RHE for Ti_3C_2-U50-Fe-800, while it decreased for C-U50-Fe-800. Lastly, Ti_3C_2-U10-Fe-800 (Fig. 5A and B) displays the lower n value with an average of 2.96, starting at 2.83 at 0.8 V *vs.* RHE and up to 3.33 at 0.4 V *vs.* RHE, which supports the fact that two processes may be at play for the ORR. Therefore, from the K–L plot and the RRDE experiments presented in Fig. 4, it can be concluded that samples Ti_3C_2-U50-Fe-800 and C-U50-Fe-800 can catalyse the ORR through an apparent ~4-electron pathway, while ORR on Ti_3C_2-U10-Fe-800 seems to occur with mixed processes. It should also be note that the calculated electron transfer number from the RRDE experiments in Fig. 4 is higher than the one deduced from K–L curves in Fig. 5, going from 3.4 at 0.8 V *vs.* RHE to 3.9 at 0.1 V *vs.* RHE. Some studies have shown that both K–L and RRDE methods have limitations when it comes to the determination of the apparent electron transfer number.[51]

To further study and understand the kinetics of the ORR in the different materials, Tafel plots were plotted and are presented in Fig. 6A. The Tafel curves of all catalysts show two slopes, one in the higher potential (lower overpotential) region and another one in the lower potential (higher overpotential) region. The region of interest, when looking at the kinetics of reaction for a catalyst is the lower overpotential region, as a minor change in potential can induce a drastic variation in current density. The slope of the Tafel plot is a great tool to evaluate the ORR kinetics on a catalyst and helps with the comparison between different materials. The calculated Tafel slopes are given in Table 4. The value for the Tafel slope obtained for Pt/C is 61 mV dec^{-1} for the low j_k region, which is characteristic of commercial Pt/C catalysts.[52] The Tafel slopes

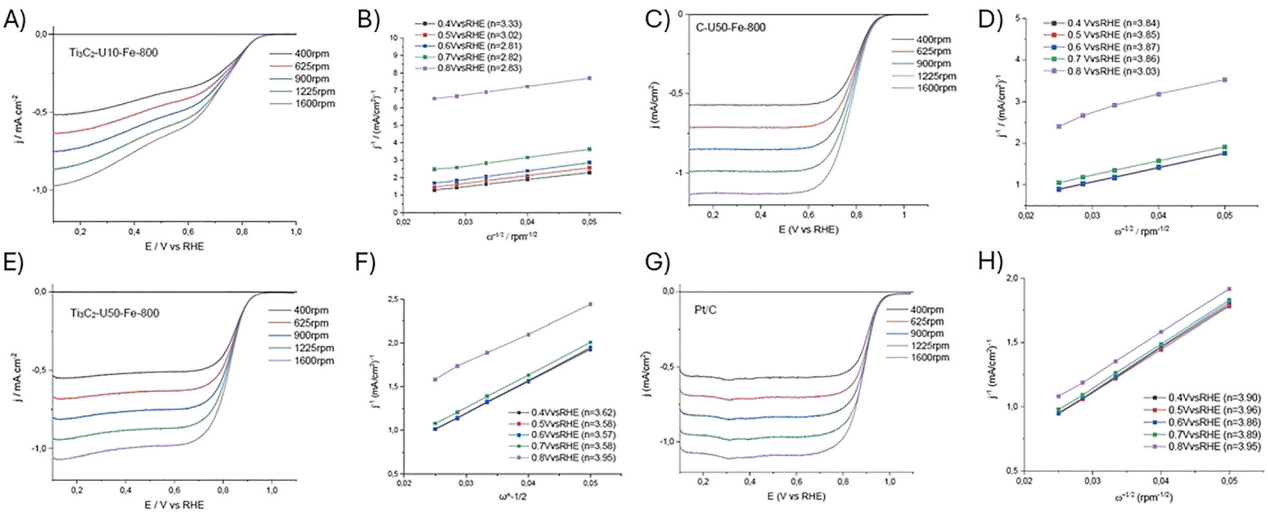

Fig. 5 Linear sweep voltammograms (LSV) at 5 mV s^{-1} at different rotation speeds in 0.1 M aerated KOH electrolyte, and Koutecky–Levich (KL) plots at potentials between 0.4 and 0.8 V *vs.* RHE (calculated n in the insets). (A) LSV of Ti_3C_2-U10-Fe-800. (B) KL plot of Ti_3C_2-U10-Fe-800. (C) LSV of Ti_3C_2-U50-Fe-800. (D) KL plot of Ti_3C_2-U50-Fe-800. (E) LSV of C-U50-Fe-800. (F) KL plot of C-U50-Fe-800. (G) LSV of Pt/XC72R (20 wt%). (H) KL plot of Pt/XC72R (20 wt%).

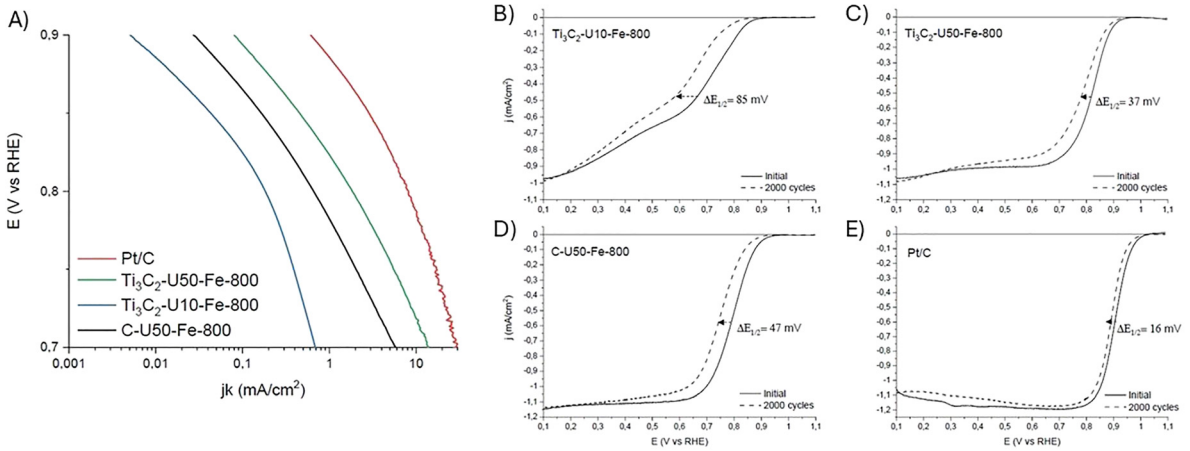

Fig. 6 (A) Tafel plots of C-U50-Fe-800, Ti_3C_2-U10-Fe-800, Ti_3C_2-U50-Fe-800 and Pt/XC72R (20 wt%). (B)–(E) Linear sweep voltammetry before and after cycling between 0.5 and 1.0 V *vs.* RHE of the different support materials: (B) Ti_3C_2-U10-Fe-800, (C) Ti_3C_2-U50-Fe-800, (D) C-U50-Fe-800, (E) Pt/C. The electrolyte is a 0.1 M aerated KOH solution.

Table 4 Summary of electrochemical properties of the samples in air saturated 0.1 M KOH electrolyte

Sample	E_{onset} (V *vs.* RHE)	j_k at 0.85 mA cm_{disk}^{-2} (mA cm^2)	j_k at 0.9 mA cm_{disk}^{-2} (mA cm^2)	n (average from KL plots)	Tafel slope (mV dec^{-1})	$\Delta E_{1/2}$ half-wave potential shift after ADT (mV)
Ti_3C_2-U10-Fe-800	0.86	0.04	0.005	2.96	89	85
Ti_3C_2-U50-Fe-800	0.93	0.47	0.08	3.66	66	37
C-U50-Fe-800	0.91	0.17	0.03	3.69	73	47
Pt/C	0.96	3.02	0.61	3.91	61	16

of the other samples are as follows: 66, 73 and 89 mV dec^{-1} for Ti_3C_2-U50-Fe-800, C-U50-Fe-800 and Ti_3C_2-U10-Fe-800 respectively. These results shows that the kinetics of ORR on Ti_3C_2-U50-Fe-800 are the best out of the materials synthesized, while Ti_3C_2-U10-Fe-800 shows poorer kinetics. Tafel slopes are also important to shed light on the reaction mechanisms that occur. Typically, values of around 60 mV dec^{-1} are observed in Pt electrodes and metal oxides, which suggest a mechanism where the second electron transfer is the rate determining step, after a fast first electron transfer, whereas values closer to 120 mV dec^{-1} suggest a mechanism where the first electron transfer to oxygen is the rate-determining step.[53] Our results show that Pt/C and Ti_3C_2-U50-Fe-800 have values close to 60 mV dec^{-1}, suggesting that the second electron transfer is the rate determining step. The other samples show higher slopes, of up to 89 mV dec^{-1}, suggesting more complex multi-step mechanisms which can be influenced by surface coverage and other factors.[53]

The kinetic current densities j_k at 0.85 and 0.9 V *vs.* RHE have been calculated and are given in Table 4. It is clearly visible from the j_k values of 3.02 and 0.61 mA cm^{-2} that Pt/C is the most active material towards the ORR. By comparing Ti_3C_2-U50-Fe-800 and C-U50-Fe-800, it can be seen that the presence of the MXene as a support has allowed for more than double the values of j_k at both 0.85 and 0.9 V *vs.* RHE, showing that Ti_3C_2-U50-Fe-800 has a better activity towards ORR than C-U50-Fe-800. Based on previous physico-chemical characterisation, this improvement towards ORR is most likely owed to the presence of MXene, which interacts with the different precursors and allows for the formation of a greater number of Fe–N_x moieties on the Ti_3C_2-U50-800 compared to the C-U50-Fe-800. Moreover, previous studies have showed that MXenes can also interact with the compounds in which it has been deposited on, leading to greater ORR activity compared to the materials without MXene support.[11,13,23] On the other hand, the MXene sample with less quantity of urea is showing poor activity towards ORR, with j_k values of 0.04 and 0.005 at 0.85 and 0.9 V *vs.* RHE respectively. Based on previous Mössbauer measurements, it can be seen that Ti_3C_2-U10-Fe-800 has slightly lower amount of Fe–N_x compared to Ti_3C_2-U50-Fe-800, but still higher than C-U50-Fe-800. Possible explanations for this difference in activity between the MXene samples may be the overall higher nitrogen content of Ti_3C_2-U50-800 compared to Ti_3C_2-U10-800 (see EDS and XPS nitrogen content measurements), providing more pyridinic N active sites towards ORR.[54] Thus, it can be concluded that the presence of MXene as support is not the only factor to consider when synthesizing the materials.

Stability of a catalyst is a very important parameter to test, as it will determine how quickly the catalyst will degrade and therefore its lifetime. Stability and degradation studies are usually done by comparing the catalyst performance before and after cycling, which is done through an ADT (accelerated durability test). These conditions were adapted from the literature,[55] with the number of cycles chosen as literature indicates most of the degradation under these conditions would occur during the first 2000 cycles.

In this work, ADT was performed by cycling the different samples between 0.5 and 1.0 V (*vs.* RHE) for 2000 cycles, sweeping at 50 mV s^{-1} rate. LSV measurements were performed post-cycling and compared to the pre-cycling LSVs, and these results for the different samples are given in Fig. 6. As expected, all post-cycling LSVs show similar onset potential compared to the pre-cycling LSV, but cycling has shifted the kinetic region of the curve toward lower potentials, which is a sign that degradation has happened in the catalyst materials. A good way to evaluate the amount of degradation of a catalyst is to measure the shift of the half-wave potential ($\Delta E_{1/2}$) of the LSV curve after the ADT compared to pre-cycling sample. From the results, the sample with the less degradation overall is Pt/C, which displays a $\Delta E_{1/2}$ of 16 mV. The half-wave potential shifts after ADT are more consequent for the Fe-containing materials, with $\Delta E_{1/2}$ of 85, 37 and 47 mV for Ti_3C_2-U10-Fe-800, Ti_3C_2-U50-Fe-800 and C-U50-Fe-800 respectively. As in previous results, the Ti_3C_2-U50-Fe-800 is the one with the least degradation out of the other three samples, and the Ti_3C_2-U10-Fe-800 is the one with the most. The slight decrease in performance in the Pt/C sample is not usually observable under these conditions and could be due to small contamination of the electrode surface by Cl^- ions leaking from the SCE.

All the electrochemical characteristics measured and discussed in this section are summarized in Table 4.

Overall, the ORR performance indicators for the different samples follow this trend: Pt/C > Ti_3C_2-U50-Fe-800 > C-U50-Fe-800 > Ti_3C_2-U10-Fe-800. Based on the physico-chemical characterisation of the materials, most of the improvement in ORR performance of Ti_3C_2-U50-Fe-800 compared to the other two materials can be explained by:

- A higher nitrogen content, which favourably formed pyridinic N species (see deconvolution of XPS N 1s spectra). Pyridinic N is well known to improve ORR activity compared to other carbonous N species.
- The choice of support material. Based on SEM and Mössbauer results, MXenes seem to have interacted with the Fe precursor and allowed some spatial confinement during the synthesis, restricting the agglomeration of Fe particles during thermal treatment and allowing for more Fe–N_x species to form.

Conclusions

The objective of this work was to show that the Fe precursor can catalyse and react with the urea decomposition products to form additional carbon species on the MXenes, as well as forming Fe and Fe–N–C species, which are known to have good ORR activities in alkaline media. The introduction of $FeCl_3$ along with urea and MXenes has proven to be effective in improving several aspects of the materials. Both Ti_3C_2-U10-Fe-800 and Ti_3C_2-U50-Fe-800 have shown ORR activity, and several factors have been found to contribute to this based on the physicochemical characterization of the samples.

Of the tested samples and excluding Pt/C, the overall activity towards ORR is as follow: Ti_3C_2-U50-Fe-800 > C-U50-Fe-800 > Ti_3C_2-U10-Fe-800. Based on the physico-chemical characterisation of the samples, several aspects have found to have an impact on this increase in activity. First, there is an increase in surface area of both Ti_3C_2-U10-Fe-800 and Ti_3C_2-U50-Fe-800 compared with the precursor MXene, as the precursor is essentially non-porous and the BET surface areas of Ti_3C_2-U10-Fe-800 and Ti_3C_2-U50-Fe-800 are 178.5 and 124.1 m^2 g^{-1} respectively. The increase can be explained by the presence of Fe species, which allowed for more urea decomposition product to react and form carbonous species on the surface of the MXenes, which increased the surface area. XRD measurements support this, with the (002) graphitic carbon peak at 26° 2θ becoming more prominent and XPS also showing an increase in the content of C. Based on SEM, it seems that the quantity of urea added during the synthesis has an influence on the morphology of the materials. Indeed, the sample containing more urea has shown to have grown CNT/CNF structures on the surface of the MXene flakes, while no CNT/CNF seems to have formed if the urea amount is too low. Based on literature, CNT/CNF growth is most likely catalysed by the presence of Fe species such as α-Fe and Fe_3C.[56]

The use of Ti_3C_2 as a support has also shown to have a positive impact on the ORR activity of the final material. This could be explained by the higher quantity of Fe–N_x formed during the synthesis when Ti_3C_2 was used as a support, while when the support was change to XC72-R the Fe–N_x content dropped. Therefore, the MXene layers played a role during the synthesis. The main hypothesis is that the MXene must have restricted the aggregation of Fe into α-Fe and Fe_3C during the thermal treatment, allowing the formation of the Fe–N_x moieties, by either interacting with the $FeCl_3$ precursor or by providing a steric restriction once the ions have been intercalated. SEM pictures seem to support this, as qualitatively the particles sizes of the Fe species visible seem to be smaller for Ti_3C_2-U50-Fe-800 compared to C-U50-Fe-800.

In conclusion, we have shown how a porous stable MXene-based structure can be achieved by intercalating Fe-containing precursors and urea within the layers, with subsequent annealing. The obtained materials show good performance when used as catalysts for the ORR in alkaline media, with sample Ti_3C_2-U50-Fe-800 showing the most promise, with an onset potential of 0.93 V *vs.* RHE, an average electron transfer number of 3.66 and a Tafel slope value of 66 mV dec^{-1}.

Conflicts of interest

There are no conflicts to declare.

Data availability

The data supporting this article have been included as part of the supplementary information (SI). The Supplementary information file contains more characterisation data, including powder X-ray diffraction, elemental analysis, details and fitting parameters for the Mössbauer spectroscopy, SEM, nitrogen adsorption data, and XPS results, details and fitting parameters. See DOI: https://doi.org/10.1039/d5ya00371g.

Acknowledgements

LB gratefully acknowledges the School of Engineering at Lancaster University for funding his PhD.

References

1 IPCC, *Climate Change 2023: Synthesis Report: Contribution of Working Groups I, II and III to the Sixth Assessment Report of the Intergovernmental Panel on Climate Change [Core Writing Team, H. Lee and J. Romero (eds.)]*. IPCC, Editor. Geneva, Switzerland, 2023.
2 I. E. Agency, *World Energy Outlook 2024*, 2024.
3 I. Staffell, *et al.*, The role of hydrogen and fuel cells in the global energy system, *Energy Environ. Sci.*, 2019, **12**(2), 463–491.
4 N. Johnson, *et al.*, Realistic roles for hydrogen in the future energy transition, *Nat. Rev. Clean Technol.*, 2025, **1**(5), 351–371.
5 Y. Yang, *et al.*, Electrocatalysis in Alkaline Media and Alkaline Membrane-Based Energy Technologies, *Chem. Rev.*, 2022, **122**(6), 6117–6321.
6 M. Naguib, *et al.*, Two-Dimensional Nanocrystals Produced by Exfoliation of Ti3AlC2, *Adv. Mater.*, 2011, **23**(37), 4248–4253.
7 Y. Gogotsi and B. Anasori, The Rise of MXenes, *ACS Nano*, 2019, **13**(8), 8491–8494.
8 C.-Y. Liu and E. Y. Li, Termination Effects of Pt/v-Tin + 1CnT2 MXene Surfaces for Oxygen Reduction Reaction Catalysis, *ACS Appl. Mater. Interfaces*, 2019, **11**(1), 1638–1644.
9 Q. Wang, *et al.*, Insights into MXenes-based electrocatalysts for oxygen reduction, *Energy*, 2022, **255**, 124465.
10 R. Yoo, *et al.*, Review—The Oxygen Reduction Reaction on MXene-Based Catalysts: Progress and Prospects, *J. Electrochem. Soc.*, 2022, **169**(6), 063513.
11 Z. Li, *et al.*, The Marriage of the FeN4 Moiety and MXene Boosts Oxygen Reduction Catalysis: Fe 3d Electron Delocalization Matters, *Adv. Mater.*, 2018, **30**(43), 1803220.
12 W.-T. Wang, *et al.*, When MOFs meet MXenes: superior ORR performance in both alkaline and acidic solutions, *J. Mater. Chem. A*, 2021, **9**(7), 3952–3960.
13 J. Chen, *et al.*, Integrating MXene nanosheets with cobalt-tipped carbon nanotubes for an efficient oxygen reduction reaction, *J. Mater. Chem. A*, 2019, **7**(3), 1281–1286.
14 L. Jiang, *et al.*, Iron-Cluster-Directed Synthesis of 2D/2D Fe–N–C/MXene Superlattice-like Heterostructure with Enhanced Oxygen Reduction Electrocatalysis, *ACS Nano*, 2020, **14**(2), 2436–2444.
15 Y.-X. Wang, *et al.*, Surface-engineered N-doped carbon nanotubes with B-doped graphene quantum dots: Strategies to develop highly-efficient noble metal-free electrocatalyst for online-monitoring dissolved oxygen biosensor, *Carbon*, 2022, **186**, 406–415.
16 Y. Wen, *et al.*, FeNC/MXene hybrid nanosheet as an efficient electrocatalyst for oxygen reduction reaction, *RSC Adv.*, 2019, **9**(24), 13424–13430.
17 L. Chen, *et al.*, Hybridization of Binary Non-Precious-Metal Nanoparticles with d-Ti_3C_2 MXene for Catalyzing the Oxygen Reduction Reaction, *ChemElectroChem*, 2018, **5**(21), 3307–3314.
18 J. Liu, *et al.*, Construction of Ti_3C_2 supported hybrid Co3O4/NCNTs composite as an efficient oxygen reduction electrocatalyst, *Renewable Energy*, 2020, **160**, 1168–1173.
19 Q. Xue, *et al.*, Mn3O4 nanoparticles on layer-structured Ti_3C_2 MXene towards the oxygen reduction reaction and zinc–air batteries, *J. Mater. Chem. A*, 2017, **5**(39), 20818–20823.
20 H. Lei, *et al.*, Strongly Coupled NiCo2O4 Nanocrystal/MXene Hybrid through In Situ Ni/Co–F Bonds for Efficient Wearable Zn–Air Batteries, *ACS Appl. Mater. Interfaces*, 2020, **12**(40), 44639–44647.
21 X. Yang, *et al.*, Multiwall carbon nanotubes loaded with MoS2 quantum dots and MXene quantum dots: Non–Pt bifunctional catalyst for the methanol oxidation and oxygen reduction reactions in alkaline solution, *Appl. Surf. Sci.*, 2019, **464**, 78–87.
22 S. L. Han, *et al.*, Multi-dimensional hierarchical CoS@MXene as trifunctional electrocatalysts for zinc-air batteries and overall water splitting, *Sci. China Mater.*, 2021, **64**(5), 1127–1138.
23 X. Yu, *et al.*, Decorating g-C3N4 Nanosheets with Ti_3C_2 MXene Nanoparticles for Efficient Oxygen Reduction Reaction, *Langmuir*, 2019, **35**(8), 2909–2916.
24 T. T. Huynh and H. Q. Pham, Defect and non-metallic doping co-engineering in two-dimensional transition-metal carbide-based electrocatalysts for renewable energy conversion, *Coord. Chem. Rev.*, 2026, **549**, 217254.
25 T. T. Huynh, N. N. Dang and H. Q. Pham, Design Strategies of 2D MXene-Based Materials for CO2 Electrolysis and Li–CO2 Batteries, *Small*, 2026, **22**(9), e13885.
26 H. Q. Pham, *et al.*, Nitrogen-doped 2D MXene-based catalysts: Synthesis, properties and applications for electrochemical hydrogen production, *Adv. Colloid Interface Sci.*, 2025, **341**, 103493.
27 M. Ghidiu, *et al.*, Conductive two-dimensional titanium carbide 'clay' with high volumetric capacitance, *Nature*, 2014, **516**(7529), 78–81.
28 P. A. Maughan, *et al.*, In Situ Investigation of Expansion during the Lithiation of Pillared MXenes with Ultralarge Interlayer Distance, *J. Phys. Chem. C*, 2021, **125**(38), 20791–20797.
29 P. A. Maughan, *et al.*, Porous Silica-Pillared MXenes with Controllable Interlayer Distances for Long-Life Na-Ion Batteries, *Langmuir*, 2020, **36**(16), 4370–4382.
30 P. A. Maughan, N. Tapia-Ruiz and N. Bimbo, In-situ pillared MXene as a viable zinc-ion hybrid capacitor, *Electrochim. Acta*, 2020, **341**, 136061.
31 M. J. Clark, *et al.*, MXene synthesis in a semi-continuous 3D-printed PVDF flow reactor, *Nanoscale Adv.*, 2025, **7**(8), 2166–2170.
32 L. Bouscarrat, G. Gaurav, R. Dawson and N. Bimbo, Urea-treated $Ti_3C_2T_z$ MXene for improved oxygen reduction reaction in alkaline fuel cells, (under review).

33 X. Sun, *et al.*, Atomic-Level Fe-N-C Coupled with Fe3C-Fe Nanocomposites in Carbon Matrixes as High-Efficiency Bifunctional Oxygen Catalysts, *Small*, 2020, **16**(6), 1906057.
34 M. Sahadat Hossain and S. Ahmed, Easy and green synthesis of TiO2 (Anatase and Rutile): Estimation of crystallite size using Scherrer equation, Williamson-Hall plot, Monshi-Scherrer Model, size-strain plot, Halder-Wagner Model, *Results Mater.*, 2023, **20**, 100492.
35 U. I. Kramm, *et al.*, Correlations between Mass Activity and Physicochemical Properties of Fe/N/C Catalysts for the ORR in PEM Fuel Cell via 57Fe Mössbauer Spectroscopy and Other Techniques, *J. Am. Chem. Soc.*, 2014, **136**(3), 978–985.
36 E. Park, *et al.*, Characterization of phases formed in the iron carbide process by X-ray diffraction, mossbauer, X-ray photoelectron spectroscopy, and Raman spectroscopy analyses, *Metall. Mater. Trans. B*, 2001, **32**(5), 839–845.
37 L. Zhong, *et al.*, 57Fe-Mössbauer spectroscopy and electrochemical activities of graphitic layer encapsulated iron electrocatalysts for the oxygen reduction reaction, *Appl. Catal., B*, 2018, **221**, 406–412.
38 M. Li, *et al.*, Element Replacement Approach by Reaction with Lewis Acidic Molten Salts to Synthesize Nanolaminated MAX Phases and MXenes, *J. Am. Chem. Soc.*, 2019, **141**(11), 4730–4737.
39 F. Cao, *et al.*, Recent Advances in Oxidation Stable Chemistry of 2D MXenes, *Adv. Mater.*, 2022, **34**(13), 2107554.
40 J. Lu, *et al.*, Tin + 1Cn MXenes with fully saturated and thermally stable Cl terminations, *Nanoscale Adv.*, 2019, **1**(9), 3680–3685.
41 D. Wilson and M. A. Langell, XPS analysis of oleylamine/oleic acid capped Fe3O4 nanoparticles as a function of temperature, *Appl. Surf. Sci.*, 2014, **303**, 6–13.
42 B. Dharmasiri, *et al.*, $Ti_3C_2T_x$ MXene coated carbon fibre electrodes for high performance structural supercapacitors, *Chem. Eng. J.*, 2023, **476**, 146739.
43 Y. Chen, *et al.*, Isolated Single Iron Atoms Anchored on N-Doped Porous Carbon as an Efficient Electrocatalyst for the Oxygen Reduction Reaction, *Angew. Chem., Int. Ed.*, 2017, **56**(24), 6937–6941.
44 W. Liu, *et al.*, Discriminating Catalytically Active FeNx Species of Atomically Dispersed Fe–N–C Catalyst for Selective Oxidation of the C–H Bond, *J. Am. Chem. Soc.*, 2017, **139**(31), 10790–10798.
45 J. H. Zagal and M. T. M. Koper, Reactivity Descriptors for the Activity of Molecular MN4 Catalysts for the Oxygen Reduction Reaction, *Angew. Chem., Int. Ed.*, 2016, **55**(47), 14510–14521.
46 S. Akula, *et al.*, Transition metal (Fe, Co, Mn, Cu) containing nitrogen-doped porous carbon as efficient oxygen reduction electrocatalysts for anion exchange membrane fuel cells, *Chem. Eng. J.*, 2023, **458**, 141468.
47 W.-J. Jiang, *et al.*, Understanding the High Activity of Fe–N–C Electrocatalysts in Oxygen Reduction: Fe/Fe3C Nanoparticles Boost the Activity of Fe–Nx, *J. Am. Chem. Soc.*, 2016, **138**(10), 3570–3578.
48 Á. García, *et al.*, Study of the evolution of FeNxCy and Fe3C species in Fe/N/C catalysts during the oxygen reduction reaction in acid and alkaline electrolyte, *J. Power Sources*, 2021, **490**, 229487.
49 J. H. Kim, *et al.*, Roles of Fe–Nx and Fe–Fe3C@C Species in Fe–N/C Electrocatalysts for Oxygen Reduction Reaction, *ACS Appl. Mater. Interfaces*, 2017, **9**(11), 9567–9575.
50 Z. Wen, *et al.*, Nitrogen-Enriched Core-Shell Structured Fe/Fe3C-C Nanorods as Advanced Electrocatalysts for Oxygen Reduction Reaction, *Adv. Mater.*, 2012, **24**(11), 1399–1404.
51 R. Zhou, *et al.*, Determination of the Electron Transfer Number for the Oxygen Reduction Reaction: From Theory to Experiment, *ACS Catal.*, 2016, **6**(7), 4720–4728.
52 X. Ge, *et al.*, Oxygen Reduction in Alkaline Media: From Mechanisms to Recent Advances of Catalysts, *ACS Catal.*, 2015, **5**(8), 4643–4667.
53 T. Shinagawa, A. T. Garcia-Esparza and K. Takanabe, Insight on Tafel slopes from a microkinetic analysis of aqueous electrocatalysis for energy conversion, *Sci. Rep.*, 2015, **5**(1), 13801.
54 K. Takeyasu, *et al.*, Role of Pyridinic Nitrogen in the Mechanism of the Oxygen Reduction Reaction on Carbon Electrocatalysts, *Angew. Chem., Int. Ed.*, 2021, **60**(10), 5121–5124.
55 M. F. Labata, *et al.*, Insights on platinum-carbon catalyst degradation mechanism for oxygen reduction reaction in acidic and alkaline media, *J. Power Sources*, 2021, **487**, 229356.
56 Z. He, *et al.*, Iron Catalysts for the Growth of Carbon Nanofibers: Fe, Fe3C or Both?, *Chem. Mater.*, 2011, **23**(24), 5379–5387.